

Implicit neural representation for change detection

Peter Naylor
RIKEN AIP
Kyoto, Japan

peter.naylor@riken.jp

Diego Di Carlo
RIKEN AIP
Kyoto, Japan

diego.dicarlo@riken.jp

Arianna Traviglia
Istituto Italiano di Tecnologia
Venice, Italy

arianna.traviglia@iit.it

Makoto Yamada
OIST
Okinawa, Japan

makoto.yamada@oist.jp

Marco Fiorucci
Istituto Italiano di Tecnologia
Venice, Italy

marco.fiorucci@iit.it

08 March 2023

Abstract

Detecting changes that occurred in a pair of 3D airborne LiDAR point clouds, acquired at two different times over the same geographical area, is a challenging task because of unmatched spatial supports and acquisition system noise. Most recent attempts to detect changes on point clouds are based on supervised methods, which require large labelled data unavailable in real-world applications. To address these issues, we propose an unsupervised approach that comprises two components: Neural Field (NF) for continuous shape reconstruction and a Gaussian Mixture Model for categorising changes. NF offer a grid-agnostic representation to encode bi-temporal point clouds with unmatched spatial support that can be regularised to increase high-frequency details and reduce noise. The reconstructions at each timestamp are compared at arbitrary spatial scales, leading to a significant increase in detection capabilities. We apply our method to a benchmark dataset of simulated LiDAR point clouds for urban sprawl-ing. The dataset offers different challenging scenarios with different resolutions, input modalities and noise levels, allowing a multi-scenario comparison of our method with the current state-of-the-art. We boast the previous methods on this dataset by a 10% margin in intersection over union metric. In addition, we apply our methods to a real-world scenario to identify illegal excavation (looting) of archaeological sites and confirm that they match findings from field experts.

1 Introduction

Nowadays, we observe the Earth through various sensors at unprecedented spatial and temporal resolutions. Thanks to these measurements named Earth Observation data, we can monitor and expand our current knowledge about our planet [37]. EO data are mainly captured through remote sensing systems mounted on satellites and flying devices, and terabytes of data are acquired daily. LiDAR data has risen in popularity

with applications in autonomous driving [23], robotics [28], urban sprawling [8], and cultural heritage [43]. This increase is threefold. Firstly, LiDAR data are highly precise (the spatial resolution is under 1m) in recording a 3D environment. Secondly, LiDAR acquisition systems are insensitive to lighting conditions. Finally, LiDAR can map terrain and uncover structures hidden by canopies. LiDAR data presents itself as point cloud data, shown in Fig. 1, and can contain millions of points depending on the sensor resolution and scanned area.

In this context, Change Detection (CD) aims to identify relevant differences in altitude on a pair of LiDAR point clouds at two different times (bi-temporal) over the same geographical area, shown in Fig. 1. CD is an active field of research because it plays an important role in monitoring global world changes and human activities, such as disasters, deforestation, urban sprawling, and human pillaging [2, 39]. This paper tackles CD for monitoring urban sprawling and identifying cultural heritage looting. Monitoring archaeological looting is paramount as looting leads to damage, misplacement or complete loss of valuable archaeological artefacts. While airborne LiDAR has become the mainstay of remote sensing archaeological reconnaissance [5, 15, 43], to the best of our knowledge, this is the first time it is applied to looting detection. Urban sprawling has been monitored by detecting both newly built and demolished buildings occurring in multi-temporal LiDAR point clouds which is essential to help landscape and city managers to promote sustainable development. This task has been widely explored in remote sensing and computer vision communities in the last decades [8].

Most existing methods process data defined on discrete regular grids and require supervised training. Feature extraction methods and Deep Neural Networks (DNN) have been both applied to CD for urban sprawling, [46, 20, 9, 45], achieving state-of-the-art performances. However, these methods require a preprocessing step to project the raw 3D LiDAR point cloud onto a 2D regular grid. The most widespread projection methods are the Digital Elevation Model (DEM) [29], and Digital

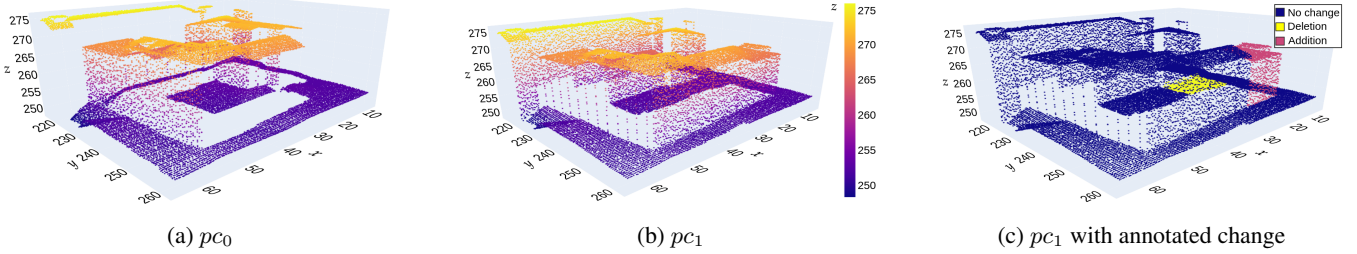


Figure 1: Simulated airborne LiDAR data for change detection of a clipped test data area.

Surface Model (DSM) [12, 25, 45]. These models are therefore limited by the correctness of the projection and memory complexity that scale with the desired resolution, making these approaches inefficient for large point clouds. In contrast, we investigate the application of CD directly to the off-grid large raw 3D LiDAR point clouds in an unsupervised manner which is particularly important for real-world applications.

We develop a novel grid-agnostic unsupervised method in a two-step approach for CD based on recent advances in DNN. In the first step, we propose to use NF, also known as Implicit Neural Representation [44] for surface reconstruction. We propose to model the changes by assuming a sparse modification of the learned field over time. The total variation loss [4] regularises and improves detection capabilities in any scenario. In the second step, we then categorise the change in altitude given by the reconstruction of the surfaces at both timestamps. We apply our method to two EO datasets. The first is an open simulated airborne LiDAR dataset consisting of 15 unique points clouds, where the goal is to identify newly built and demolished buildings. The underlying task of this objective is a tool to understand the landscape better and help city managers promote sustainable development. The second dataset is a pair point cloud over Kulen, an area of Cambodia with several archaeological structures. We aim to detect precise locations of illegal excavation sites to collect historical material culture, i.e. looting.

The contributions of our work are the following:

- Applying DNN for unsupervised CD from 3D LiDAR;
- Using unsupervised sparse regularisation over time for CD in the shape reconstruction loss;
- Outperforming state-of-the-art by more than 10%;
- Applying CD for looting monitoring activities with field experts' feedback.

2 Related works

The off-grid and noisy nature of point clouds collected by a LiDAR system detrimentally impacts the performances of change detection methods. Moreover, weather conditions and remote sensor trajectory may differ for two measurements at different timestamps, leading to spatial unmatching support. Despite this, supervised methods for CD can achieve great performances even in challenging noisy data. However, their us-

age is still limited to a few real-world applications due to the prohibitive cost of collecting and labelling training datasets.

For these reasons, unsupervised methods represent an attractive alternative. Such methods can be broadly classified into two categories [8]: those based on distance computation [16, 40], and those based on optimal transport [7, 14]. Distance-based methods, such as C2C [16], and M3C2 [22, 40] divide the point cloud via octrees, estimate the surface normal and orientation to calculate pair-wise euclidean distances. Alternatively, optimal transport-based methods estimate a distance based on the projection matrix of the first cloud onto the second. In both cases, the actual changes are then classified via empirical thresholding, or the OTSU method [30]. These methods have been developed and applied to the only available airborne LiDAR dataset for building change detection [8]. However, datasets usually contain millions of points because they are acquired with high-spatial resolution acquisition systems [38]. The previous methods do not scale well with the data size and have to subdivide the point cloud for analysis.

Other methods for unsupervised CD do not use raw 3D LiDAR data directly. Instead, they used 2D images obtained by projecting the 3D point clouds on a 2D regular grid, e.g., for DEM and DSM [47]. Due to the grid's regularity, ordering and consistency, these projected 2D images are ideally suited for convolutional operations. Hence, convolutional neural network-based architectures can be applied to the 2D digital models for building CD [46, 45, 39]. However, these projections lead to precision loss of the LiDAR data as the height measurements are interpolated to output the DSM or the DEM [8]. To the best of our knowledge, the work we presented here is the first study investigating the use of DNNs for unsupervised CD from raw point cloud data.

Novel DNN models, called NFs [44], have tackled off-grid point cloud analysis [34, 20] and 3D surface reconstruction [42, 41, 18] in both supervised and unsupervised way. The NFs are *coordinate-based* deep learning models that map coordinates to descriptive a field (e.g. occupancy, density or colour). The resulting function is called the Implicit Neural Representation of the field, which can be estimated by fitting observation and inducing desired properties by application-based regularisation terms.

A native limitation of NF is their poor capability of capturing high-frequency details of the surface, referred to as spectral bias [42]. To address this, positional encoding and Random Fourier Features (RFF) [35] of the input coordinates have be-

come standard practice. This allowed to apply NF to a new plethora of applications and methodologies, such as 3D shape reconstruction from sparse images, animation of human bodies and faces, as well as video coding [44]. Moreover, RFF have improved Physics-Informed Neural Networks (PINNs) [36], which are similar coordinate-based DNNs trained to fit observations while solving partial differential equation evaluated with network’s backpropagation algorithm [19, 10].

An alternative approach to surpass the frequency bias is SIREN [41], where the standard nonlinearities are replaced with periodic sine functions. Such architectures show a very low reconstruction error, both in fitting the target field and its gradient with respect to the input. SIRENs have become standard backbone networks for both NF and physics-informed neural networks [44]. Despite their success, SIRENs suffer from difficulties in training as they are prone to overfit or being stuck in local minima, for which careful parameter tuning is required. These issues have been addressed in subsequent works [13, 24], where novel architectures have been proposed claiming easier training and faster convergence. Nevertheless, in practice, SIREN’s performance depends on the applications. As reported in this work, SIREN does not consistently outperform RFF-based architecture.

Most of the NF-based models for 3D reconstruction recover the object shape by minimising the signed distance between any given point and the closest surface [32]. Then, the associated NF is a function of the three spatial coordinates. A positive sign implies the point lies outside the object and vice versa. The shape contours are then found by checking the 0 iso-line of the learned function. Neural Unsigned Distance Fields [6] remove the sign from the distance function and encode continuous locations for a stronger regularisation, leading to better reconstruction. However, these methods are inappropriate for CD with LiDAR data as they require normals vectors to reconstruct the 3D shape [18], which are unavailable in LiDAR data. Moreover, as we will discuss in Section 3, urban sprawling can be reasonably approximated by a continuous function over a 2D space.

3 Method

We want to detect changes in two LiDAR point clouds with unsupervised methods. A cloud point at time t will be denoted by $\mathcal{X}_t \subset \mathbb{R}^3$ where each element is a 3D coordinate, i.e. $(x, y, z) \in \mathcal{X}_t$. We will denote by $t_0 = 0$ and $t_1 = 1$ the two timestamps for which we wish to detect change. If the support of \mathcal{X}_0 and \mathcal{X}_1 match, we naturally define the addition of an element by a positive difference, i.e. the 2D point (x, y) is of the label "Addition" if the associated altitudes: $z_1 - z_0 > \alpha$, where z_t corresponds to the altitude at time t and with α a fixed scalar. Similarly, we can define the "Deletion" class by a negative difference. However, this is not directly applicable to LiDAR point clouds as the supports do not match because of different acquisition conditions. To fix the support, some have used projection methods [8] and optimal transport [14]. In the current paper, we fix the support matching by estimating a sur-

face from the cloud point, allowing us to interpolate and query any spatial point. In other words, we reconstruct the surface at a given time point. In particular, we can then compute the difference to find additions or deletions. It is important to note that we are estimating a function that maps a position to an altitude, which is different from the actual cloud point. Some points will share the same (x, y) but have different altitudes due to the inclination of the LiDAR emitter and the verticality of elements in the maps, especially if these are buildings.

3.1 Regression model

We denote by f_θ an MLP model with learnable parameters θ . Given an input vector \mathbf{v} , we estimate the density:

$$f_\theta : V \rightarrow \mathbb{R}$$

$$\mathbf{v} \mapsto z$$

where $V = \mathbb{R}^2$ in our first formulation. Naturally, we can independently reconstruct the first and second cloud. We sum the baseline method in the following detection formula:

$$\Delta z(x, y) = (f_{\theta_1} - f_{\theta_0})(x, y). \quad (1)$$

Here θ_t corresponds to the set of DNN parameters to reconstruct the surface at time t that are optimised by minimising the mean squared error (MSE) between the estimated and observed altitude.

A more compact and efficient representation is possible where we modify the input $\mathbf{v} \in \mathbb{R}^3$ of the network to incorporate time. In particular, we learn a single model with parameters θ , and the detection formula is modified to:

$$\Delta z(x, y) = f_\theta(x, y, t_1) - f_\theta(x, y, t_0) \quad (2)$$

A priori, it is not evident to know in advance which method is better suited for a given dataset. In some configurations of the simulated datasets, \mathcal{X}_0 and \mathcal{X}_1 are not drawn from the same distribution, which could potentially be harmful to the single model. Therefore we investigate the benefits of a single model as opposed to two. In the following sections, we will describe in more detail the different regularisations and model specificities we apply to improve reconstruction.

3.2 Random Fourier Features

We map the input \mathbf{v} to a higher dimensional space with RFF to help capture higher frequencies in the surface. It has been shown that this projection is crucial for estimating high frequencies for a better reconstruction and that the gaussian mapping performs best [42]. For a fixed model, RFF are defined as follows:

$$B \in \mathbb{R}^{M \times 3}, \forall (i, j), B_{ij} \sim \mathcal{N}(0, \sigma)$$

$$\gamma_B(\mathbf{v}) = [\cos(2\pi B\mathbf{v}), \sin(2\pi B\mathbf{v})]$$

The size of B depends on the size of \mathbf{v} , and here we supposed $\mathbf{v} \in \mathbb{R}^3$. The mapping size M and the scale σ are two hyperparameters that need tuning.

3.3 Network architecture

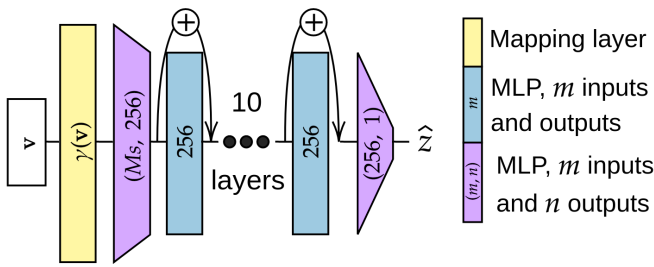


Figure 2: Neural network model, ‘skip-ten-only’.

We propose several network architectures comprising MLP layers, different activations, and skip layers in Table A.2 of the Appendix. We show in Fig. 2 a particular model that we name ‘skip-ten-only’. In particular, the network size will depend on the data complexity. We use skip layers allowing a better gradient flow [17]. The activation functions will be ReLU or hyperbolic tangent (tanh), as tanh allows the resulting f_θ to be \mathcal{C}^∞ , we do not use any activation layers for the last layer.

We use a similar architecture to the one presented in Fig. 2 for the SIREN methods. We use skip layers and tanh activation, including the final layer. We allow the final model to choose the architecture for both methods by making it a hyperparameter.

3.4 Total variation norm

The total variation norm, defined as $\sum |u_{i+1} - u_i|$ is a standard regularisation scheme for sequential like data [4]. It is also helpful to smooth spatial patterns, as a sudden altitude change should be penalised. Such a scheme has been generalised to a continuous version by enforcing that the resulting gradient of the function f_θ be sparse over the spatial coordinates [36]. It is possible to add to the loss function the regularisation term $\mathcal{R}_{TV} = |\frac{\partial f_\theta}{\partial x}| + |\frac{\partial f_\theta}{\partial y}|$.

3.5 Time difference

Similarly to the discrete total variation norm, we can enforce that the change over time be sparse, which indicates to the DNN that most points do not change over time, but we will allow some to change. To enforce such a constraint, we add the following regularisation to the loss function: $\mathcal{R}_{TD} = |f_\theta(x, y, t_1) - f_\theta(x, y, t_0)|$. This regularisation is only possible when the input v contains time, and therefore it cannot be applied where we reconstruct the surface for two models (1). This regularisation over time is very similar to the total variation norm over the temporal domain. We stress that shape reconstruction does not need this regularisation term, and this is only a CD regulariser. In particular, adding this term to the loss allows us to fuse the information from both cloud points more efficiently and enables the point clouds to benefit from each other mutually.

3.6 SIREN

From an architectural point of view, the SIREN network [41] is a simple modification of an MLP where standard activation functions, e.g. ReLU and tanh, are continuous sine functions. This substitution enables the modelling of a continuous complicated signal without the need for explicit upsampling in various domains. The SIREN network can then be described by

$$f(\mathbf{x}) = \mathbf{W}_n(g_{n-1} \circ g_{n-2} \circ \dots \circ g_0 \mathbf{x}) + \mathbf{h}_n, \quad (3)$$

where $g_i(\mathbf{h}_i) = \sin(\mathbf{W}_i \mathbf{h}_i + \mathbf{b}_i)$.

SIREN operates as a composition of sinusoidal transformations recalling the principle behind RFF. In fact, it has been shown that positional encoding with RFF is equivalent to periodic nonlinearities with one hidden layer as the first DNN layer [3]. Good initialisation of the weights is critical for their successful training. To avoid saturation of the sine activations, a scalar hyperparameter σ is introduced to scale the layers’ weights, like for RFF.

3.7 Unsupervised labelling of Δz

Once the surface reconstruction is performed, we have access to Δz given by equation (1) or (2). The OTSU threshold method has been used to separate binary sources [30, 27] for change detection. However, in our case, we have three sources to distinguish and use a Gaussian Mixture Model (GMM) with three components [26]. We show in Fig. 3 the application of GMM to Δz for a small clipped sample. This step can be tricky depending on the distribution of Δz as the GMM will divide the distribution into three, regardless of the shape of the distribution. It could potentially lead to a random score.

4 Experimental setting

4.1 Simulated dataset

We use the publicly simulated airborne LiDAR dataset for CD [8]. Even if this dataset is simulated, it mimics true data with different noise levels and sensors used in practice. Five simulation configurations are given: 1 - Low resolution – low noise, 2 - high resolution – low noise, 3 - low resolution – high noise, 4 - photogrammetry and 5 - multi-sensor. The photogrammetry setting is low resolution, high noise and tight scan angle for each timestamp. They mimic satellite acquisition. The multi-sensor simulation is characterised by pc_0 and pc_1 having different resolutions and noise levels. pc_0 is low resolution and high noise, whereas pc_1 is high resolution and low noise. In this situation $\#pc_1 \gg \#pc_0$ which is different to other subsets where $\#pc_1 \approx \#pc_0$. $\#$ denotes the cardinality of the set. Each configuration is divided into training and testing datasets. We will only apply the method to the testing sets as the methods used are unsupervised. For each testing configuration, three simulated datasets exist where the ground truth is different for each. The testing set comprises three different geographical areas of the city of Lyon in France [8]. Only the

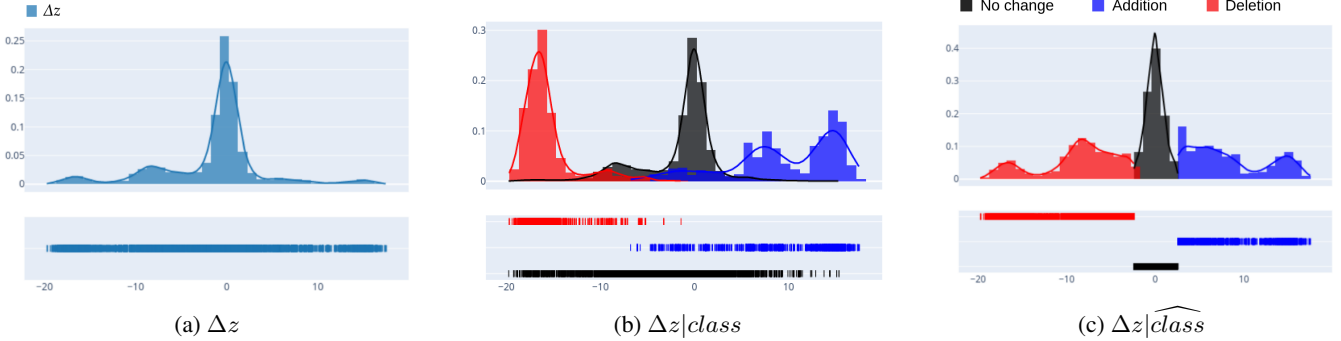


Figure 3: Distribution of Δz and with predicted and true class label. This distribution was computed on a small subset with a single DNN (i.e. equation (2)) with the RFF and no regularisation.

second cloud point pc_1 is annotated with additions and deletion changes and will be used to evaluate the methods. In Fig. 1c, we overlay pc_1 with the annotation.

4.2 Metrics

The minimised MSE used to cross-validate training will not be used for evaluation. Due to the noise level, a good performance on this metric will not imply a good reconstruction. Indeed an MSE of 0 implies that the model perfectly reconstructs the data and the noise.

Intersection over union uses predicted and true labels: $IoU(P, G) = \frac{P \cap G}{P \cup G}$. This metric is very sensitive to small changes, especially when the ground truth is small, like in our situation. The IoU will be measured after applying the GMM to Δz . In particular, a low score could mean that the GMM is unfit for converting the differences into labels or that the surface reconstruction failed.

Average AUC will be computed to highlight good-performing methods irrespective of the GMM results. We compute the standard AUC over three settings: addition vs no addition, deletion vs no deletion and change vs no change. In the last setting, we use $|\Delta z|$.

4.3 Training procedure

In detail, we will describe how we train our network f_θ given a point cloud. When a single network is used, cloud points pc_0 and pc_1 are concatenated, and the input dimension is three. With no loss of generality, we will consider that we have a single point cloud pc of dimension two or three. We normalise the point cloud to be in $[-1; 1]$ on each axis. We randomly split the dataset in two where 80% is retained for training and the other 20% is used for validation. We minimise and backpropagate through the training loss and evaluate the MSE performance on the validation. We use Optuna [1] to find the best set of hyperparameters via bayesian optimisation that minimises the validation MSE. The tuned hyper-parameters are the model architecture, the learning rate, the batch size, the scale of the gaussian mapping, the scalars associated with the regularisation terms λ_{TD} , and λ_{TV} . When we use the SIREN model,



Figure 4: IoU results for different feature mapping methods for every LiDAR airborne simulated dataset.

we also optimise the scale size by multiplying the signal in the sinusoidal activation function, the number of layers, and the number of hidden units for each layer. We use the optimisation method Adam [21] wrapped with the Layer-wise Adaptive Rate Scaling (LARS) [31] that enables the use of an enormous batch size that for us is essential to carry out our experiments in a reasonable time. To speed up computation, we set the number of epochs to 50, use learning rate decay and early stopping. To compute the TV norm, we sample random elements from pc that we corrupt with noise and backpropagate their prediction to the input [36].

5 Results and discussion

5.1 Feature mapping

In Fig. 4, we show the IoU results between the different mapping methods: no feature mapping, RFF and SIREN. In Fig. A.1 of the Appendix, we show the results for the AUC metric. In Fig. 5, we show some resulting crops trained with no feature mapping, RFF and SIREN. We show additional crops as well as the whole map for data (3) in Fig. A.2 and A.3 of the Appendix. For both metrics, IoU and AUC, RFF outperforms SIREN and the default configuration by a fair margin. In terms

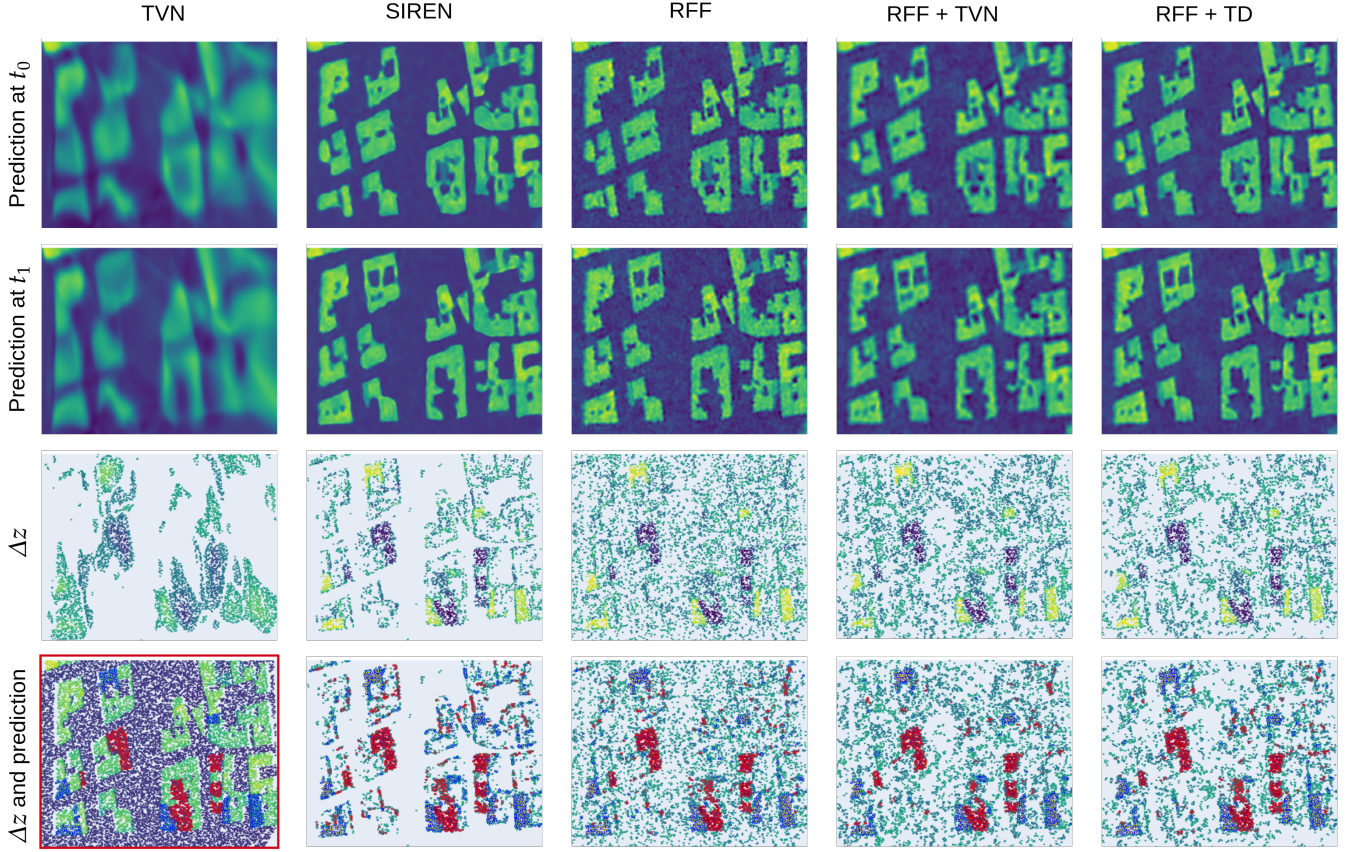


Figure 5: Visualisation of a crop where in each column we show a different method comprising a single DNN trained on dataset (3). In the two first rows, we reconstruct the surface along a regular grid for timestamp t_0 and t_1 . In the third row we show the difference Δz on the support of \mathcal{X}_1 and in the fourth row we overlay these difference with the predicted labels from the GMM, we filter out points where $|\Delta z| < 2$. Each column shows a different method. In the final row and in the first column we show the true cloud point overlaid with the ground truth. To compare fairly, the color map ranges from dark purple, 160m altitude, to yellow, 205m, for the first two rows and from -30m to 30m for the visualisation of Δz .

of average performance with standard deviation, RFF reaches an IoU of 0.53 ± 0.12 and an AUC of $0.976 \pm 7 \times 10^{-3}$ and, SIREN 0.39 ± 0.10 and $0.959 \pm 2.8 \times 10^{-2}$, and not using any mapping reaches 0.30 ± 0.15 and $0.959 \pm 3.8 \times 10^{-2}$. Please check Table A.1 in the Appendix for the deconvolution of the values reported. From the visualisation in Fig. 5, no feature mapping leads to a reconstruction where the building delimitation is unclear and fuzzy. SIREN gives the sharpest reconstruction with close to no noise between the buildings. Conversely, SIREN’s projection onto the support of the second timestamp, given in the final column, is subject to many false positives along building boundaries. The RFF method produces distinctive buildings, like SIREN, but with a noisier output. However, the number of false positives in the final row is smaller. This ablation study shows the necessity of feature mapping to achieve good IoU and, therefore, a good reconstruction. Capturing high-frequencies is essential to our current problem due to the verticality of buildings.

5.2 Hyper-parameter influence

In Fig. 6, we show a study on the regularisation parameter λ_{TD} and λ_{TVN} for both RFF, in darker and SIREN, in lighter colours. We measure the IoU and RMSE for both and compare them to the setting without penalty. Naturally, a too-strong penalty damages the performance, and a too-low value leads to a negligible performance. Only for the method using RFF and TD regularisation do we see a 6% improvement in IoU compared to the baseline. This optimal λ_{TD} does not necessarily correspond to a minimal RMSE, metric used for the validation scheme. Similarly to Section 5.1, RFF features obtain better performance on both metrics and a more stable reconstruction noticeable by a lower RMSE and smaller confidence intervals.

The literature reports better reconstruction for SIREN over the RFF methods. However, in our situation, SIREN gives lower performances in terms of IoU and MSE. SIREN suffers more from the mathematical formulation given in Section 3, which is ill-posed because of many points on the sides of the buildings. As SIREN induces qualitatively a better reconstruction, i.e. sharper edges and less noise. Having samples

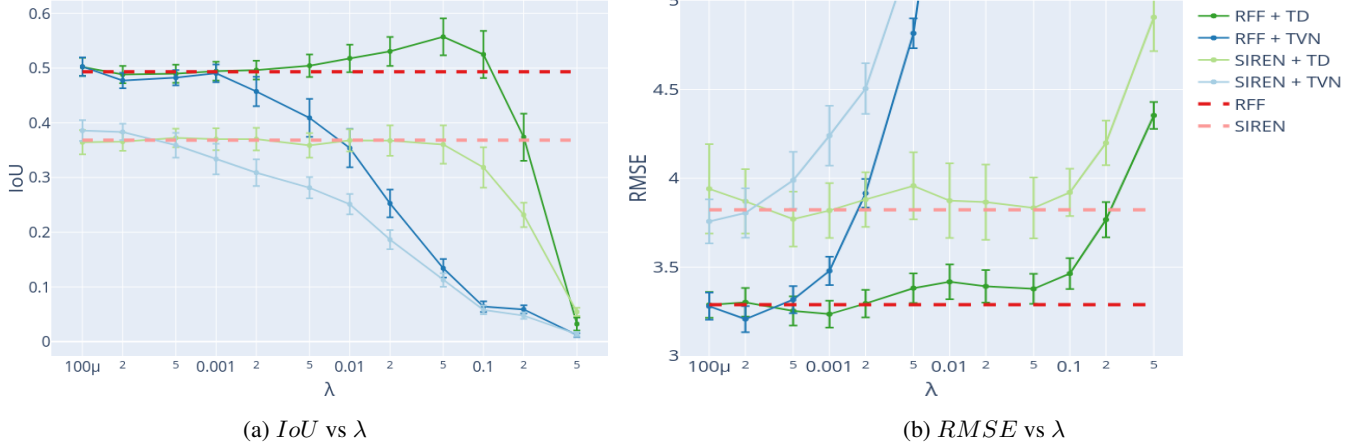


Figure 6: Influence of parameter λ , referring to either λ_{TD} or λ_{TVN} , with respect to the IoU or reconstruction metric. We show 95% confidence intervals for each estimator. Each point followed other hyper-parameter selection procedures (20 attempts to minimise the reconstruction) and was repeated 20 times. In red dashes, we show the model with λ set to 0.

from the point cloud sharing similar geographical coordinates but radically different altitudes (along the verticality of the building) leads SIREN to slightly misplace the boundaries of the buildings, leading to many false positives along their edges, and hence a lower *IoU*. SIREN’s MSE is higher, as the MSE penalises false positives more strongly as they correspond to larger differences between the ground truth and the prediction. The sharper edges of SIREN, compared to RFF, are harmful in terms of *IoU* and MSE. In other words, SIREN’s reconstruction is sharper and, due to noise, wrongly estimates the building size. In contrast, the RFF method has softer edges, i.e. less overfitting induced by capturing fewer high-frequencies. This leads to a better mean error along the building edges and, therefore, to a lower minimisation of the MSE and fewer false positives.

5.3 Comparison to state of the art

In Table 1, we benchmark methods on the simulated dataset and compare the previous state-of-the-art in unsupervised detection, M3C2 [22], OT [14] and SIREN to our method. RFF outperforms the other methods by a large margin, about 13% and 8% in *IoU* over the previous state of the art. In addition, the previous state-of-the-art maximised the *IoU* with respect to a threshold, whereas our method is completely unsupervised. For example, SIREN is still an improvement over the previous state-of-the-art even though the results do not show this because the metric report for SIREN is fairer than those reported.

The experiments favour the use of one single function for the reconstruction of the surface for both timestamps. We notice a difference of 2% in *IoU* between using a single model and two models when no regularisation is applied.

The regularisation \mathcal{R}_{TD} shows the most improvement in terms of *IoU* compared to \mathcal{R}_{TV} with a difference of over 3%. Expectedly, the best-achieving model uses both, which should perform at least as well as the non-regularised version. In

practice, it could disregard any regularisations by setting the respective scalar to 0 during the cross-validation. In the following, we use the model with one single model, RFF and both regularisation, named model ‘S+RFF+TVN+TD’.

5.4 Application to Cultural heritage

The two-fold purpose of using LiDAR point clouds to identify looting activities is to validate model ‘S+RFF+TVN+TD’ on real (non-simulated) bi-temporal pairs of LiDAR point clouds and assess its capability to detect looting, which is a pressing problem on a global scale. We processed one bi-temporal pair of Lidar points clouds acquired over the Phnom Kulen region (Cambodia), where there are temples and ancient dams of Angkor-era largely obscured by thick and closed canopies. Still, LiDAR deals well with this environment thanks to its capability to penetrate landscapes covered by continuous vegetation. The first cloud pc_0 was acquired in 2012, and the second cloud pc_1 in 2015. Fig. 7 shows the changes related to looting detected by model ‘S+RFF+TVN+TD’. Archaeologists drew the red bounding box to identify an area where looting occurred. The archaeologists verified the predicted changes through visual inspection and confirmed that all the looting pits inside the bounding box were correctly identified. The false positive in the top right part can be easily filtered due to the 20 meters diameter, which is too big to be considered a looting pit.

6 Conclusion

The amount of Earth observation acquired with 3D LiDAR data is rising exponentially, which opens up the possibility of monitoring human activity through change detection algorithms. In particular, we focused on urban planning and identifying looting activities. Thanks to advances in DNN, we can now estimate and reconstruct large areas with high precision

Data	M3C2 [22]	OT [14]	None	SIREN	RFF					
			S+TVN	S	D	D+TVN	S	S+TVN	S+TD	S+TVN+TD
(1)	0.2987	0.4065	0.3722	0.4014	0.5013	0.4468	0.5249	0.5587	0.5473	0.4968
(2)	0.5373	0.552	0.4522	0.5398	0.5739	0.5933	0.5645	0.6117	0.6034	0.5952
(3)	0.3872	0.3926	0.3311	0.3857	0.4654	0.4317	0.5187	0.4694	0.5400	0.5333
(4)	0.3501	0.3989	0.3354	0.3901	0.4862	0.497	0.5138	0.5110	0.5340	0.5399
(5)	0.3778	0.4817	0.3797	0.4048	0.4255	0.4316	0.4295	0.4326	0.4055	0.4717
Avg	0.3902	0.4463	0.3741	0.4243	0.4904	0.4800	0.5102	0.5167	0.5260	0.5274

Table 1: Comparaison to state-of-the-art on the IoU metric, we only report the best configuration when no feature mapping and SIREN. We show in red the best performing model in each row. D denotes the model with two DNN given by equation (1) and S the model with a single DNN given by equation (2). The complete table can be found in Table A.1 of the Appendix.

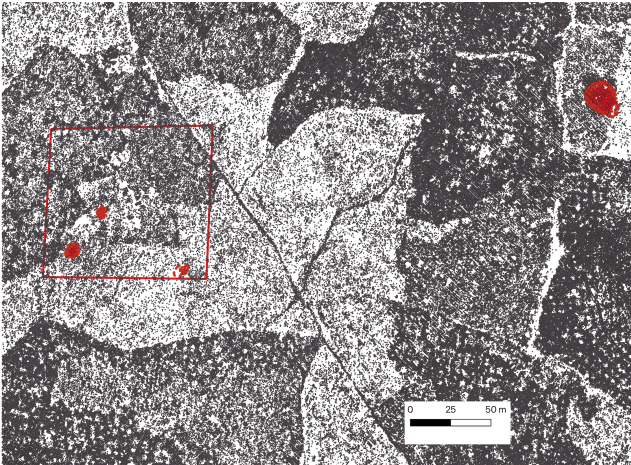


Figure 7: Detection of looting pits on a bi-temporal pair of LiDAR point clouds. The ground truth bounding box identified the geographical area where looting occurred. The red points represent detected looting pits.

that allows passing the reconstructed surfaces to downstream tasks. However, the amount of training data and their discrete modelling limits their application to real scenarios. To address these issues, we propose a novel unsupervised grid-agnostic scheme for change detection based on surface reconstruction and clustering, which achieves 0.5274% IoU , surpassing previous state-of-the-art by 10% on average. Moreover, we demonstrated in this paper that RRF mapping outperforms SIREN for change detection on point cloud data acquired from LiDAR and allows us to identify looting activity correctly.

Code availability

The code is made fully available at the following URL: [NN-4-change-detection](#) The code runs efficiently with hyperparameter selection thanks to the Optuna [1] package. We use GPU computation with PyTorch [33] and combine each experiment into a pipeline with Nextflow [11] for reproducibility.

Acknowledgement

MY was supported by MEXT KAKENHI 20H04243 and partly supported by MEXT KAKENHI 21H04874. MF was supported by the European Union’s Horizon 2020 research and innovation programme under grant agreement No 101027956. We thankful Damian Evans for providing us with a pair of LiDAR point clouds for looting identification. We are also thankful for the RAIDEN computing system and its support team at the RIKEN AIP, which we used for our experiments.

References

[1] Takuya Akiba, Shotaro Sano, Toshihiko Yanase, Takeru Ohta, and Masanori Koyama. Optuna: A next-generation hyperparameter optimization framework. In *Proceedings of the 25th ACM SIGKDD international conference on knowledge discovery & data mining*, 2019. 5, 8

[2] A. Asokan and J. Anitha. Change detection techniques for remote sensing applications: a survey. *Earth Science Informatics*, 12, 2019. 1

[3] Nuri Benbarka, Timon Höfer, Andreas Zell, et al. Seeing implicit neural representations as fourier series. In *Proceedings of the IEEE/CVF Winter Conference on Applications of Computer Vision*, pages 2041–2050, 2022. 4

[4] Kevin Bleakley and Jean-Philippe Vert. The group fused lasso for multiple change-point detection. *arXiv preprint arXiv:1106.4199*, 2011. 2, 4

[5] Adrian S. Z. Chase, Diane Z. Chase, and Arlen F. Chase. *LiDAR for Archaeological Research and the Study of Historical Landscapes*, pages 89–100. Springer International Publishing, Cham, 2017. 1

[6] Julian Chibane, Gerard Pons-Moll, et al. Neural unsigned distance fields for implicit function learning. *Advances in Neural Information Processing Systems*, 33:21638–21652, 2020. 3

[7] Nicolas Courty, Rémi Flamary, Devis Tuia, and Thomas Corpetti. Optimal transport for data fusion in remote sensing. In *2016 IEEE international geoscience and remote sensing symposium (IGARSS)*, pages 3571–3574. IEEE, 2016. 2

[8] Iris de Gélis, Sébastien Lefèvre, and Thomas Corpetti. Change detection in urban point clouds: An experimental comparison with simulated 3d datasets. *Remote Sensing*, 13(13):2629, 2021. 1, 2, 3, 4

[9] Iris De Gélis, Sébastien Lefèvre, Thomas Corpetti, Thomas Ristorcelli, Chloé Thénoz, and Pierre Lassalle. Benchmarking change detection in urban 3d point clouds. In *2021 IEEE International Geoscience and Remote Sensing Symposium (IGARSS)*, pages 3352–3355. IEEE, 2021. 1

[10] Diego Di Carlo, Dominique Heitz, and Thomas Corpetti. Post processing sparse and instantaneous 2d velocity fields using physics-informed neural networks. In *20th International Symposium On Application Of Laser And Imaging Techniques To Fluid Mechanics*, 2022. 3

[11] Paolo Di Tommaso, Maria Chatzou, Evan W Floden, Pablo Prieto Barja, Emilio Palumbo, and Cedric Notredame. Nextflow enables reproducible computational workflows. *Nature biotechnology*, 35(4):316–319, 2017. 8

[12] Mustafa Erdogan and Altan Yilmaz. Detection of building damage caused by van earthquake using image and digital surface model (dsm) difference. *International Journal of Remote Sensing*, 40(10):3772–3786, 2019. 2

[13] Rizal Fathony, Anit Kumar Sahu, Devin Willmott, and J Zico Kolter. Multiplicative filter networks. In *International Conference on Learning Representations*, 2021. 3

[14] Marco Fiorucci, Peter Naylor, and Makoto Yamada. Optimal transport for change detection on lidar point clouds, 2023. 2, 3, 7, 8

[15] Marco Fiorucci, Wouter Verschoof-van der Vaart, Paolo Soleni, Bertrand Saux, and Arianna Traviglia. Deep learning for archaeological object detection on lidar: New evaluation measures and insights. *Remote Sensing*, 14:1694, 03 2022. 1

[16] Daniel Girardeau-Montaut, Michel Roux, Raphaël Marc, and Guillaume Thibault. Change detection on points cloud data acquired with a ground laser scanner. *International Archives of Photogrammetry, Remote Sensing and Spatial Information Sciences*, 36(part 3):W19, 2005. 2

[17] Kaiming He, Xiangyu Zhang, Shaoqing Ren, and Jian Sun. Deep residual learning for image recognition. In *Proceedings of the IEEE conference on computer vision and pattern recognition*, pages 770–778, 2016. 4

[18] Zhangjin Huang, Yuxin Wen, Zihao Wang, Jinjuan Ren, and Kui Jia. Surface reconstruction from point clouds: A survey and a benchmark. *arXiv preprint arXiv:2205.02413*, 2022. 2, 3

[19] George Em Karniadakis, Ioannis G Kevrekidis, Lu Lu, Paris Perdikaris, Sifan Wang, and Liu Yang. Physics-informed machine learning. *Nature Reviews Physics*, 3(6):422–440, 2021. 3

[20] Abderrazzaq Kharroubi, Florent Poux, Zouhair Ballouch, Rafika Hajji, and Roland Billen. Three dimensional change detection using point clouds: A review. *Geomatics*, 2(4):457–485, 2022. 1, 2

[21] Diederik P Kingma and Jimmy Ba. Adam: A method for stochastic optimization. *arXiv preprint arXiv:1412.6980*, 2014. 5

[22] Dimitri Lague, Nicolas Brodin, and Jérôme Leroux. Accurate 3d comparison of complex topography with terrestrial laser scanner: Application to the rangitikei canyon (nz). *ISPRS journal of photogrammetry and remote sensing*, 82:10–26, 2013. 2, 7, 8

[23] You Li and Javier Ibanez-Guzman. Lidar for autonomous driving: The principles, challenges, and trends for automotive lidar and perception systems. *IEEE Signal Processing Magazine*, 37(4):50–61, 2020. 1

[24] David B Lindell, Dave Van Veen, Jeong Joon Park, and Gordon Wetzstein. Bacon: Band-limited coordinate networks for multiscale scene representation. In *Proceedings of the IEEE/CVF Conference on Computer Vision and Pattern Recognition*, pages 16252–16262, 2022. 3

[25] Xuzhe Lyu, Ming Hao, and Wenzhong Shi. Building change detection using a shape context similarity model for lidar data. *ISPRS International Journal of Geo-Information*, 9(11), 2020. 2

[26] Geoffrey J McLachlan and Kaye E Basford. *Mixture models: Inference and applications to clustering*, volume 38. M. Dekker New York, 1988. 4

[27] Peter Naylor, Marick Laé, Fabien Reyal, and Thomas Walter. Segmentation of nuclei in histopathology images by deep regression of the distance map. *IEEE transactions on medical imaging*, 38(2):448–459, 2018. 4

[28] Julian Nubert, Etienne Walther, Shehryar Khattak, and Marco Hutter. Learning-based localizability estimation for robust lidar localization. In *2022 IEEE/RSJ International Conference on Intelligent Robots and Systems (IROS)*, pages 17–24. IEEE, 2022. 1

[29] Unal Okyay, Jennifer Telling, Craig L. Glennie, and William E. Dietrich. Airborne lidar change detection: An overview of earth sciences applications. *Earth-Science Reviews*, 198:102929, 2019. 1

[30] Nobuyuki Otsu. A threshold selection method from gray-level histograms. *IEEE transactions on systems, man, and cybernetics*, 9(1):62–66, 1979. 2, 4

[31] Chunmyong Park, Heungsuk Lee, Myungryong Jeong, Woonhyuk Baek, and Chiheon Kim. torchlars, A LARS implementation in PyTorch. <https://github.com/kakaobrain/torchlars>, 2019. 5

[32] Jeong Joon Park, Peter Florence, Julian Straub, Richard Newcombe, and Steven Lovegrove. DeepSDF: Learning continuous signed distance functions for shape representation. In *Proceedings of the IEEE/CVF conference on computer vision and pattern recognition*, pages 165–174, 2019. 3

[33] Adam Paszke, Sam Gross, Francisco Massa, Adam Lerer, James Bradbury, Gregory Chanan, Trevor Killeen, Zeming Lin, Natalia Gimelshein, Luca Antiga, Alban Desmaison, Andreas Kopf, Edward Yang, Zachary DeVito, Martin Raison, Alykhan Tejani, Sasank Chilamkurthy, Benoit Steiner, Lu Fang, Junjie Bai, and Soumith Chintala. PyTorch: An imperative style, high-performance deep learning library. In *Advances in Neural Information Processing Systems 32*, pages 8024–8035. Curran Associates, Inc., 2019. 8

[34] Charles R Qi, Hao Su, Kaichun Mo, and Leonidas J Guibas. Pointnet: Deep learning on point sets for 3d classification and segmentation. In *Proceedings of the IEEE conference on computer vision and pattern recognition*, pages 652–660, 2017. 2

[35] Ali Rahimi and Benjamin Recht. Random features for large-scale kernel machines. *Advances in neural information processing systems*, 20, 2007. 2

[36] Maziar Raissi, Paris Perdikaris, and George E Karniadakis. Physics-informed neural networks: A deep learning framework for solving forward and inverse problems involving nonlinear partial differential equations. *Journal of Computational Physics*, 378:686–707, 2019. 3, 4, 5

[37] S Salcedo-Sanz, P Ghamisi, M Piles, M Werner, L Cuadra, A Moreno-Martínez, E Izquierdo-Verdiguier, J Muñoz-Marí, Amirhosein Mosavi, and G Camps-Valls. Machine learning information fusion in earth observation: A comprehensive review of methods, applications and data sources. *Information Fusion*, 63:256–272, 2020. 1

[38] Brent Schwarz. Lidar: Mapping the world in 3D. *Nature Photonics*, 4(7):429–430, July 2010. 2

[39] Wenzhong Shi, Min Zhang, Rui Zhang, Shanxiong Chen, and Zhao Zhan. Change detection based on artificial intelligence: State-of-the-art and challenges. *Remote Sensing*, 12(10), 2020. 1, 2

[40] Sara Shirowzhan, Samad ME Sepasgozar, Heng Li, John Trinder, and Pingbo Tang. Comparative analysis of machine learning and point-based algorithms for detecting 3d changes in buildings over time using bi-temporal lidar data. *Automation in Construction*, 105:102841, 2019. 2

[41] Vincent Sitzmann, Julien N.P. Martel, Alexander W. Bergman, David B. Lindell, and Gordon Wetzstein. Implicit neural representations with periodic activation functions. In *Proc. NeurIPS*, 2020. 2, 3, 4

[42] Matthew Tancik, Pratul Srinivasan, Ben Mildenhall, Sara Fridovich-Keil, Nithin Raghavan, Utkarsh Singhal, Ravi Ramamoorthi, Jonathan Barron, and Ren Ng. Fourier features let networks learn high frequency functions in low dimensional domains. *Advances in Neural Information Processing Systems*, 33:7537–7547, 2020. 2, 3

[43] Wouter B. Verschoof van der Vaart. *Learning to look at LiDAR: combining CNN-based object detection and GIS for archaeological prospection in remotely-sensed data*. PhD thesis, Leiden University, 2022. 1

[44] Yiheng Xie, Towaki Takikawa, Shunsuke Saito, Or Litany, Shiqin Yan, Numair Khan, Federico Tombari, James Tompkin, Vincent Sitzmann, and Srinath Sridhar. Neural fields in visual computing and beyond. In *Computer Graphics Forum*, volume 41, pages 641–676. Wiley Online Library, 2022. 2, 3

[45] Zhenchao Zhang, George Vosselman, Markus Gerke, Claudio Persello, Devis Tuia, and Michael Ying Yang. Detecting building changes between airborne laser scanning and photogrammetric data. *Remote Sensing*, 11(20), 2019. 1, 2

[46] Zhenchao Zhang, George Vosselman, Markus Gerke, Devis Tuia, and Michael Ying Yang. Change detection between multimodal remote sensing data using siamese cnn. *ArXiv*, abs/1807.09562, 2018. 1, 2

[47] Benjamin Štular, Žiga Kokalj, Krištof Oštir, and Laure Nuninger. Visualization of lidar-derived relief models for detection of archaeological features. *Journal of Archaeological Science*, 39(11):3354–3360, 2012. 2

Supplementary: Implicit neural representation for change detection

We show in the Supplementary Material results of all the methods applied to each data configuration in Table A.1. We summarise all the possible tables chosen that we optimise from in Table A.2. In addition, we give the AUC plot between RFF, SIREN and no feature mapping in Fig. A.1. Finally, we show an additional output crop from the training on data configuration (3) in Fig. A.3 and the whole map in Fig. A.2.

Data	D	D+TVN	S	S+TD	S+TD+TVN	TVN	Data	D	D+TVN	S	S+TD	S+TD+TVN	TVN
(1)	0.9012	0.8861	0.9699	0.9200	0.9664	0.9547	(1)	0.2373	0.2365	0.2114	0.1936	0.3526	0.3722
(2)	0.9721	0.9710	0.9868	0.9839	0.9882	0.9868	(2)	0.3824	0.3722	0.4672	0.4512	0.4872	0.4522
(3)	0.9104	0.8507	0.9553	0.9572	0.9600	0.9640	(3)	0.2627	0.2076	0.3175	0.3031	0.3149	0.3311
(4)	0.8993	0.8734	0.9563	0.9571	0.8296	0.9612	(4)	0.2124	0.2053	0.3519	0.3234	0.2323	0.3354
(5)	0.9306	0.9287	0.9780	0.9773	0.8652	0.9742	(5)	0.2035	0.1992	0.3132	0.2635	0.1724	0.3797
Avg	0.9227	0.9020	0.9692	0.9591	0.9219	0.9682	Avg	0.2597	0.2442	0.3322	0.3069	0.3119	0.3741

(a) AUC for no feature mapping							(b) IoU for no feature mapping						
Data	D	D+TVN	S	S+TD	S+TD+TVN	TVN	Data	D	D+TVN	S	S+TD	S+TD+TVN	TVN
(1)	0.9811	0.9810	0.9818	0.9804	0.9858	0.9843	(1)	0.5012	0.4467	0.5249	0.5473	0.4967	0.5586
(2)	0.9818	0.9819	0.9834	0.9809	0.9867	0.9826	(2)	0.5738	0.5932	0.5645	0.6033	0.5952	0.6116
(3)	0.9762	0.9776	0.9748	0.9743	0.9796	0.9805	(3)	0.4654	0.4316	0.5187	0.5399	0.5333	0.4694
(4)	0.9763	0.9759	0.9762	0.9766	0.9793	0.9814	(4)	0.4862	0.4969	0.5138	0.5340	0.5399	0.5110
(5)	0.9754	0.9792	0.9764	0.9683	0.9773	0.9804	(5)	0.4255	0.4315	0.4295	0.4055	0.4717	0.4325
Avg	0.9782	0.9791	0.9785	0.9761	0.9818	0.9818	Avg	0.4904	0.4800	0.5103	0.5260	0.5274	0.5166

(c) AUC for RFF							(d) IoU for RFF						
Data	D	D+TVN	S	S+TD	S+TD+TVN	TVN	Data	D	D+TVN	S	S+TD	S+TD+TVN	TVN
(1)	0.9780	0.9745	0.9774	0.9749	0.9777	0.9804	(1)	0.4147	0.3845	0.4014	0.3812	0.3599	0.4307
(2)	0.9813	0.9779	0.9844	0.9824	0.9793	0.9830	(2)	0.5255	0.4440	0.5397	0.4908	0.4395	0.4843
(3)	0.9702	0.9745	0.9755	0.9641	0.9660	0.9627	(3)	0.4084	0.3993	0.3857	0.4291	0.3723	0.3836
(4)	0.9716	0.9795	0.9699	0.9748	0.9740	0.9721	(4)	0.3777	0.3833	0.3901	0.3725	0.4013	0.4107
(5)	0.9759	0.9774	0.9754	0.9326	0.9748	0.9737	(5)	0.3865	0.3796	0.4047	0.2957	0.3744	0.3553
Avg	0.9754	0.9768	0.9765	0.9658	0.9744	0.9744	Avg	0.4226	0.3981	0.4243	0.3939	0.3895	0.4129

(e) AUC for SIREN							(f) IoU for SIREN						
Data	D	D+TVN	S	S+TD	S+TD+TVN	TVN	Data	D	D+TVN	S	S+TD	S+TD+TVN	TVN
(1)	0.4147	0.3845	0.4014	0.3812	0.3599	0.4307	(1)	0.4147	0.3845	0.4014	0.3812	0.3599	0.4307
(2)	0.5255	0.4440	0.5397	0.4908	0.4395	0.4843	(2)	0.5255	0.4440	0.5397	0.4908	0.4395	0.4843
(3)	0.4084	0.3993	0.3857	0.4291	0.3723	0.3836	(3)	0.4084	0.3993	0.3857	0.4291	0.3723	0.3836
(4)	0.3777	0.3833	0.3901	0.3725	0.4013	0.4107	(4)	0.3777	0.3833	0.3901	0.3725	0.4013	0.4107
(5)	0.3865	0.3796	0.4047	0.2957	0.3744	0.3553	(5)	0.3865	0.3796	0.4047	0.2957	0.3744	0.3553
Avg	0.4226	0.3981	0.4243	0.3939	0.3895	0.4129	Avg	0.4226	0.3981	0.4243	0.3939	0.3895	0.4129

Table A.1: Performance each data configuration for AUC and IoU. D denotes the model with two DNN given by equation (1) and S the model with a single DNN given by equation (2).

Models													
default	default-BN	default-L	skip-double	skip-L-double	skip-XL-double	skip-ten	skip-ten-only	skip-twenty	Input $\gamma(\mathbf{v})$				
Input $\gamma(\mathbf{v})$													
			FC-1024		FCS-1024 ($\times 2$)	FCS-1024 ($\times 4$)							
			FC-512	FCS-512 ($\times 2$)	FCS-512 ($\times 2$)	FCS-512 ($\times 4$)	FCS-512 ($\times 10$)						
FC-256	FC-256 + BN	FC-256	FCS-256 ($\times 2$)	FCS-256 ($\times 2$)	FCS-256 ($\times 3$)	FCS-256	FCS-256 ($\times 10$)	FCS-256 ($\times 20$)					
FC-128	FC-128 + BN	FC-128	FCS-128	FCS-128 ($\times 2$)	FCS-128 ($\times 2$)	FCS-128							FCS-128 ($\times 2$)
FC-64	FC-64 + BN	FC-64	FCS-64	FCS-64 ($\times 2$)	FCS-64 ($\times 2$)	FCS-64							FCS-64 ($\times 2$)
Linear mapping to a 1 dimensional output													

Table A.2: Neural Network models. FC denotes fully connected layers with a given activation. BN denotes batch normalisation. FCS denotes fully connected layers with a skip layer. For the transition when downsampling the dimension for fully connected skip layers, we add a simple FC that maps from one dimension to the other.

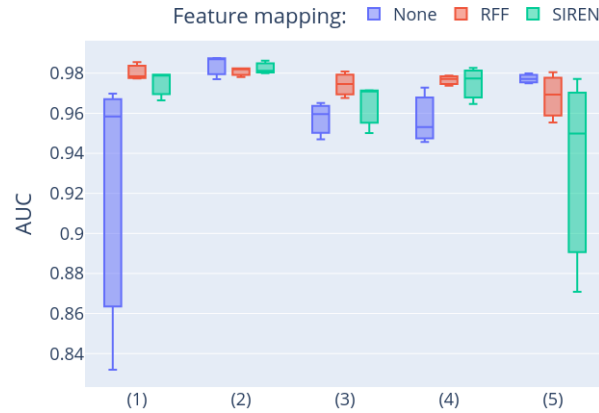


Figure A.1: AUC results for different feature mapping methods for every LiDAR airborne simulated dataset.

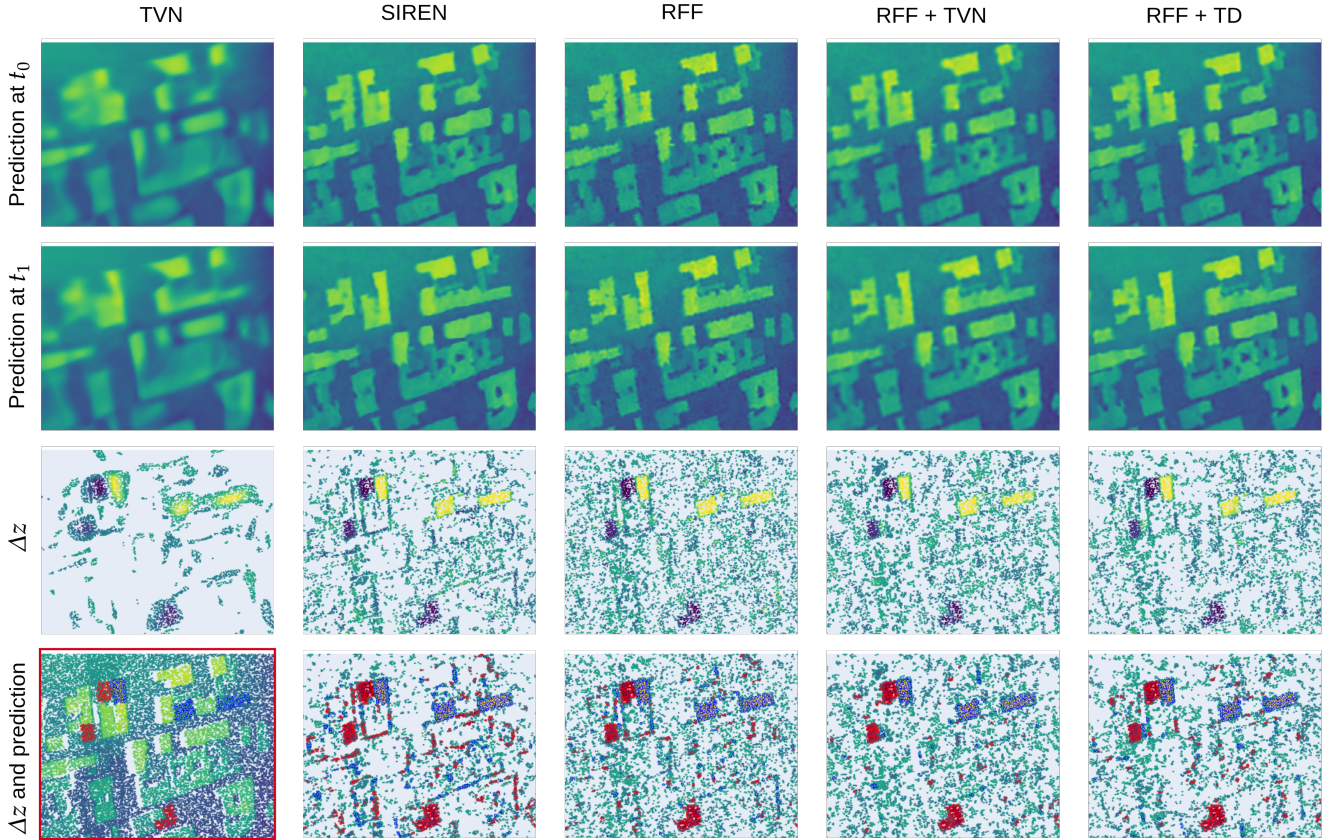


Figure A.2: Visualisation of a crop number 2 where in each column we show a different method comprising a single DNN applied. In the two first rows, we have the reconstruction of the surface along a regular grid for timestamp t_0 and t_1 . In the third row, we show the difference Δz on the support of \mathcal{X}_1 and in the fourth row we overlay these difference with the predicted labels from the GMM, we filter out points where $|\Delta z| < 2$. Each column shows a different method. In the final row and in the first column we show the true cloud point overlaid with the ground truth. To compare fairly, we range the color map from dark purple, 160m altitude, to yellow, 245m, for the first two rows and from -30m to 30m for the visualisation of Δz .

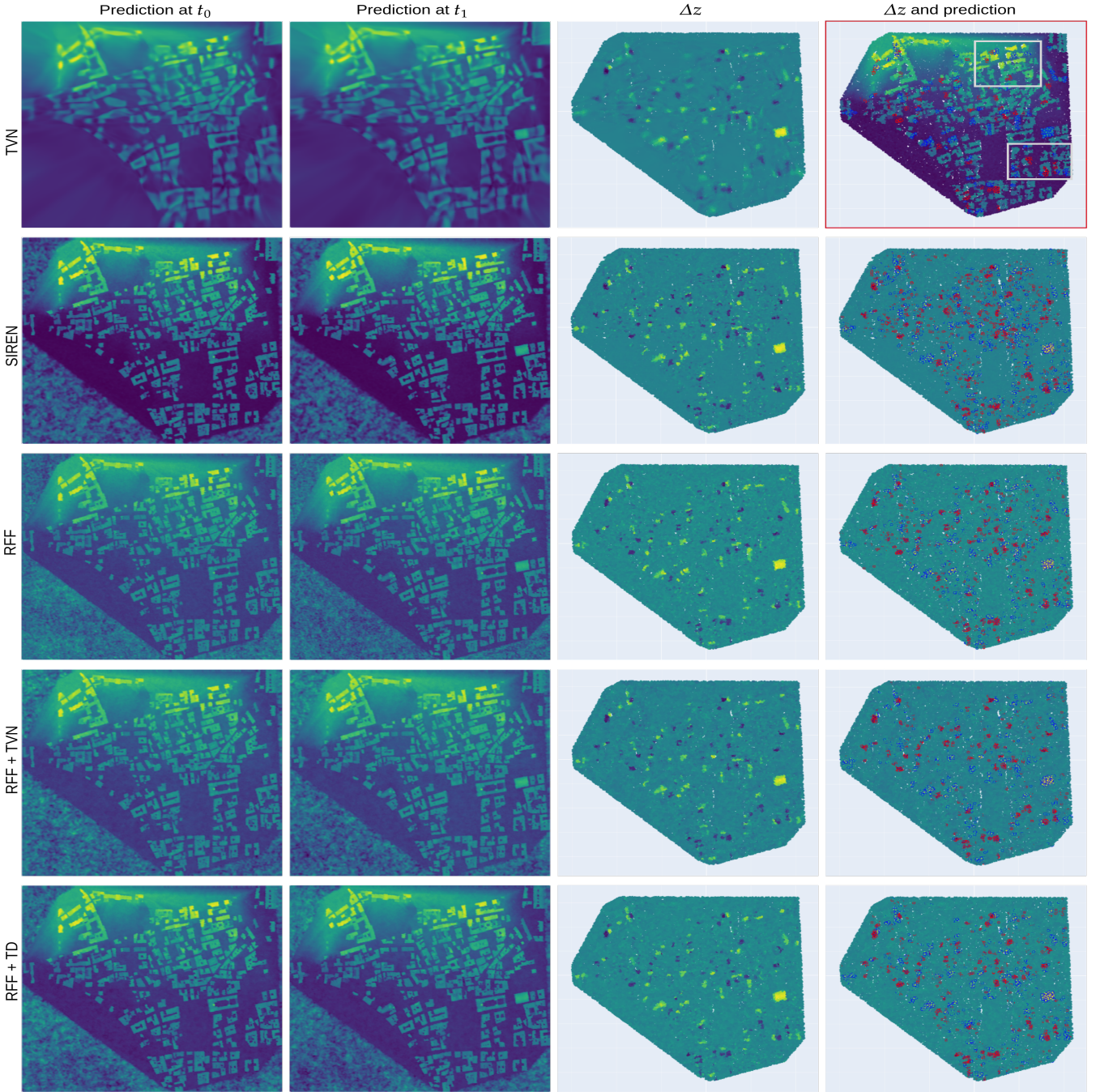


Figure A.3: Visualisation of the whole map where in each row we show a different method comprising a single DNN. In the two first columns, we have the reconstruction of the surface along a regular grid for timestamp t_0 and t_1 . In the third column, we show the difference Δz on the support of \mathcal{X}_1 and in the fourth column we overlay these difference with the predicted labels from the GMM. Each column shows a different method. In the first row and in the last column we show the true cloud point overlaid with the ground truth. In addition, we show where the crops where the other visualising crops were extracted from. To compare fairly, we range the color map from dark purple, 160m altitude, to yellow, 245m, for the first two rows and from -30m to 30m for the visualisation of Δz .